2022 American Control Conference (ACC)
Atlanta, USA, June 8-10, 2022

Optimal Control of Microgrid Lithium-ion Energy Storage using Pontryagin's Minimum Principle

Kevin Moy[1] and Simona Onori[1], *Senior Member, IEEE*

***Abstract*— Microgrids are energy systems that are able to supply power reliably in the face of instability on the main electric grid, increasingly driven by the effects of anthropogenic climate change. Microgrids are powered by diesel generators, energy storage, and renewable energy resources such as photovoltaics, to supply power to loads. Lithium-ion batteries (LIBs) are currently the dominant grid-scale energy storage technology and leading candidate for deployment in microgrids. An optimal control problem can be formulated regarding the optimal energy management of the LIB and other microgrid components, with the goal of minimizing the fuel consumption of the diesel engine. In this paper, Pontryagin's Minimum Principle (PMP) is used to solve the optimal energy management problem where the LIB is modeled through an equivalent circuit model. A semi-empirical model is used to assess the degradation of the LIB under the resulting optimal control. PMP is applied to a variety of initial and final outage conditions taken from real-world scenarios, resulting in different impacts on LIB degradation and fuel consumption.**

***Index Terms*— Pontryagin's Minimum Principle, microgrid, optimal control, equivalent circuit model**

I. Introduction

As the impacts of anthropogenic climate change increase, so do the frequency and intensity of severe weather events, including hurricanes, extreme heat waves, flooding, and wildfires [1]. Such weather events can adversely impact the stability of the electric grid, as was evident during the Texas grid outage caused by a severe winter storm in February 2021, causing millions to lose power and ultimately leading to the deaths of hundreds of people [2]. In California, nine of the twenty largest wildfires and five of the twenty deadliest wildfires have occurred between 2017 and 2020 alone [3]. In particular, the interplay between wildfires and the electrical grid is complicated: Wildfires threaten electrical infrastructure, leading to power instabilities; on the other hand, improperly maintained electrical equipment can lead to the start of wildfires, as was the case for the deadly Camp wildfire in 2018 [4]. This led to the California Public Utilties Commission instituting the Public Safety Power Shutoff (PSPS) program, which allows utilities to preemptively shut off power to communities during high wildfire risk conditions, e.g. high temperatures and strong winds.

Microgrids are a promising solution to the severe weather/power instability problem [5]. They can be off-grid, where the microgrid is permanently electrically isolated from the *macrogrid* (defined as the rest of the electrical grid, external to the microgrid), or grid-tied, where the microgrid is normally connected to the macrogrid, and may electrically isolate itself from the macrogrid during periods of grid instability. This paper addresses the scenario of a grid-tied microgrid that is isolated from the macrogrid during a particularly severe PSPS grid outage event in October 2019, when thousands of electricity customers served by the Pacific Gas and Electric (PG&E) utility in Northern California lost power for up to three days [6]. We formulate an optimization problem to control the dispatch (charge and discharge) of a lithium-ion battery energy storage system (LIB) in order to balance supply and demand within the microgrid, while minimizing diesel fuel consumption. This optimal control problem is formulated and solved using Pontryagin's Minimum Principle (PMP).

The research presented within this paper is supported by the Bits and Watts Initiative within the Precourt Institute for Energy at Stanford University.

[1]Energy Resources Engineering Department, Stanford University, Stanford, CA 94305 USA (e-mail: kmoy14@stanford.edu; sonori@stanford.edu).

II. Literature Review

PMP for the energy management optimal control problem has been previously studied in depth for hybrid electric vehicles (HEVs), providing a formulation for real-time optimal control strategies. In particular, PMP for minimizing HEV fuel consumption has been shown to be equivalent to the previously-proposed equivalent consumption minimization strategy (ECMS) [7]. This PMP formulation is readily applicable to microgrid energy storage; as in HEVs, the goal is to minimize consumption of fuel by an engine used to supply power by instead dispatching energy storage resources to meet the requested power demand. ECMS for HEV has been widely studied using a zeroth-order equivalent-circuit model (ECM) for the battery [8]–[10]. In such studies, a "charge-sustaining" mode of operation is employed, during which the battery operates within a small state of charge (SOC) window. In this operation mode, the open-circuit voltage and internal resistance are approximately constant with respect to SOC and the problem costate also remains constant, further simplifying the optimization. Over the past several years PMP has been applied to grid-scale energy storage. In [11], PMP is used to formulate a sub-optimal control strategy which balances a hybrid battery/supercapacitor energy storage system within a grid-tied microgrid for the goal of minimizing power consumed from the macrogrid, and this control strategy is also compared to a more traditional frequency-based one. In [12], PMP is employed to optimally dispatch battery energy storage to minimize fuel consumption for a generic system equivalent to an off-grid microgrid, but is reformulated as a shortest-path method in terms of the evolution of stored energy in the battery from its initial to final state, which is extended in [13] to derive an optimal control strategy

978-1-6654-5196-3/$31.00 ©2022 AACC

for energy storage systems with nonlinear power conversion efficiency losses. All three papers simply model the battery as a "bucket of electrons" which can freely store and release energy as needed, without modelling any of the physical operating characteristics of the battery. In [14], PMP is part of a hierarchical control framework, representing the lowest level real-time control of an LIB in a 100% clean energy (off-grid) microgrid. The LIB is modelled with an ECM; however, the dependence of battery voltage and internal resistance on SOC is neglected, as in the HEV energy management formulations above. This paper extends the existing literature for energy management control of grid-scale energy storage by leveraging laboratory data from prior lithium-ion cell testing to include the dependence of operating characteristics (i.e. open circuit voltage and internal resistance) on battery SOC into the costate dynamics in the PMP problem formulation. This problem formulation is applied to the specific use-case of a grid-tied microgrid that is islanded during an outage, optimally controlling the dispatch of the LIB with the goal of minimizing fuel consumption. Finally, this paper provides an analysis of the impacts of changing the boundary conditions (final state, initial and final time) on the optimal control solution as well as the resulting LIB degradation and diesel fuel consumption reduction.

III. Problem Description

A. Microgrid System

The microgrid system modelled in this paper is inspired by an existing microgrid at the Blue Lake Rancheria in Humboldt County, California, USA, which includes a 1MWAC (megawatts AC) genset, 420kWAC (kilowatts AC) solar PV array, and a 500kWAC/950kWh LIB, and supports a community with a peak load of 754kWAC [15]. In this paper, the microgrid components are scaled down to accommodate the data available for the 457kWAC genset in [16], and are summarized in Table I. A detailed description of the component models and their construction follows in Section IV.

TABLE I: Components of the microgrid modelled in this paper

Name	Rated (Peak) Power [kWAC]	Rated Energy [kWh]
Diesel Genset	475	-
Load	350	-
Solar PV Array	210	-
LIB	250	475

B. Outage Conditions

This paper focuses on the PSPS event from October 2019 in Northern California, for which power from the macrogrid was unavailable for customers between Oct. 9 and Oct. 12 [6], during which the Blue Lake Rancheria microgrid successfully provided power to its community [17]. Within the PSPS, four outage phases were rolled out to different customers within the PG&E service territory. These are shown in Table II, with outage times rounded to the nearest 0.25 hour (15-minute) interval. During the outage, power is unavailable from the macrogrid, and power flow within the microgrid at all times is prioritized according to the following. The solar PV generation can be used to either supply the load, or to charge the LIB. The genset can only be used to support the load if the solar PV and LIB cannot supply enough power to the load, i.e. the LIB is charged only off of the available solar PV and not the genset. On the other hand, if the solar PV output exceeds that of the load consumption and LIB charging, then the excess power is curtailed, without penalty. With this, the usage of renewable energy resources (solar PV and LIB) are prioritized over the genset usage. Explicitly, given solar PV generation $pv(t)$, LIB dispatch $u(t)$, and load consumption $l(t)$ at time t, all in AC power of units kWAC, we define the residual power P_{rd} as $P_{rd}(t)) = [l(t) - \max\{0, u(t)\}] - [pv(t) + \min\{u(t), 0\}]$, where $u(t)$ is positive when the LIB is discharging, and negative when the LIB is charging. Then, the genset power output $dg(t)$ is determined by $dg(t) = \max\{P_{rd}(t), 0\}$. The curtailed solar PV generation $pv_{curt}(t)$ is given as $pv_{curt}(t) = -\min\{P_{rd}(t), 0\}$. A diagram of all possible power flows for $pv(t)$, $l(t)$, $u(t)$, and $dg(t)$ is shown in Fig. 1.

TABLE II: PSPS Outages for October 9-12 2019 [6]

Phase	Start Time	End Time	Outage Length [hr]
1	Oct. 9 2019, 00:00	Oct. 12 2019, 17:45	89.75
2	Oct. 9 2019, 15:15	Oct. 12 2019, 10:15	67
3	Oct. 9 2019, 22:30	Oct. 12 2019, 12:30	62
4	Oct. 10 2019, 09:45	Oct. 12 2019, 05:30	43.75

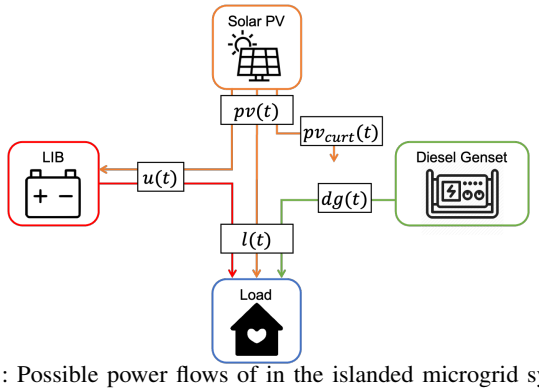

Fig. 1: Possible power flows of in the islanded microgrid system modelled in this paper. Arrows denote the flow of power, and the colors denote the origin of the power. $u(t)$ is positive when the LIB is discharging to the load, and negative when the LIB is charging from the solar PV.

Further assumptions on outage conditions: In this paper, we assume that the outage times in Table II are fixed and known to the microgrid. As the start time of the outage is known, we assume that the microgrid can prepare ahead of the outage start time by pre-charging the LIB to an initial SOC SOC_{UB} to maximize its available stored energy. We also assume that the microgrid will exit the outage at some final SOC SOC_f, so that the microgrid can be prepared for any subsequent outages.

IV. Microgrid Component Models

A. Load Model

The microgrid load consumption is constructed from data obtained from Pecan Street Inc. Dataport, which includes residential load consumption data from several locations in the United States [18]. Within the Pecan Street Inc. Dataport, residences in the Berkeley and Oakland areas in California, USA were selected, as these homes were geographically closest to Blue Lake Rancheria. Within these locations, 18 homes were found to have a complete year's worth of 15-minute consumption data. The load data were aggregated and multiplied by a factor of 10 to form the microgrid load consumption, representing 180 residential homes.

B. Solar Photovoltaic Array Model

The solar PV generation data are obtained from the System Advisor Model (SAM) developed by the National Renewable Energy Laboratory [19], which incorporates local weather data (wind, temperature, and insolation), the panels and inverter used in the microgrid solar PV array, and the total kWAC rating of the array. SAM uses these inputs to model the array power generation output for each hour in the year. The panels and inverter modelled were the same used in the Blue Lake Rancheria microgrid, as presented in [16]. The generation data were upsampled to 15-minute data to match the temporal resolution of the load.

C. Diesel Generator Model

The size and operating characteristics of the genset are obtained from existing test data collected by the Alaska Center for Energy and Power for a genset rated at 457 kWAC [16], for which fuel efficiency in kWh/L was measured at various load (genset power output) setpoints. By dividing the load by the fuel efficiency, the fuel consumption in L/hr at each load kWAC setpoint are obtained. The diesel fuel consumption $\dot{m}_f(dg(t))$ is then approximated by a polynomial function of genset power output

$$\dot{m}_f(dg(t)) = 1.23 \times 10^{-4} dg(t)^2 + 0.20 dg(t) + 16.36 \quad (1)$$

D. LIB Model

The LIB pack is modelled as a set of identical NMC lithium-ion cells electrically connected as s cells in series and p cells in parallel. The LIB pack is then connected to the LIB inverter, which converts the LIB pack DC power into AC power to interact with the rest of the microgrid. The cells are modelled using experimental data from [20], which used LG Chem INR21700-M50 NMC lithium-ion cells of nominal voltage $V_{cell,nom} = 3.63$V and nominal capacity $Q_{nom} = 4.85$Ah.

1) Pack Sizing: s and p are determined based on the nominal voltage and capacity of the cells, as well as the specifications of the LIB inverter with DC voltage range of 530V - 830V, rated power $P_{inv} = 250$kWAC, and DC-AC conversion efficiency $\eta = 0.975$ [21]. Using Kirchhoff's voltage law, the cell DC voltage, V_{cell}, and the pack DC voltage, V_{pack}, are related by the following equation

$$V_{pack}(t) = sV_{cell}(t) \quad (2)$$

Similarly, the cell DC current, I_{cell}, and the pack DC current, I_{pack}, are related using Kirchhoff's current law $I_{pack}(t) = pI_{cell}(t)$. The LIB dispatch AC power $u(t)$ is determined from the pack DC current, the pack DC voltage, and the inverter efficiency η, as $u(t) = \eta^{\mathrm{sgn}(u(t))} V_{pack}(t) I_{pack}(t)$. We assume that each identical cell contributes the same amount of power in the pack. Therefore, $u(t)$ is a function of cell power P_c, i.e. $u(t) = \eta^{\mathrm{sgn(u(t))}} spP_c(t)$. where

$$P_c(t) = V_{cell}(t) I_{cell}(t) \quad (3)$$

The pack rated energy E_{nom} can be calculated from $V_{cell,nom}$ and Q_{nom} as

$$E_{nom} = spV_{cell,nom}Q_{nom} \quad (4)$$

First, s is chosen so that the pack voltage remains within the limits of the LIB inverter. In particular, the pack voltage cannot exceed the LIB inverter upper DC voltage limit of 830V. Using Equation 2 with $V_{pack} = 830$V and $V_{cell,nom} = 3.63$V yields $s = 228$.

Then, p is chosen so that $E_{nom} = 475$kWh, as in Table I. Using Equation 4 with $s = 228$, $V_{cell,nom} = 3.63$V, and $Q_{nom} = 4.85$Ah yields $p = 118$.

2) Cell model: Each cell is modelled with a zeroth-order ECM, shown in Fig. 2.

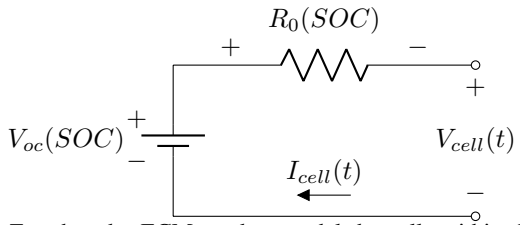

Fig. 2: Zeroth-order ECM used to model the cells within the LIB pack.

For applied cell current $I_{cell}(t)$, the cell voltage $V_{cell}(t)$ is

$$V_{cell}(t) = V_{oc}(SOC) - R_0(SOC) I_{cell}(t) \quad (5)$$

From Equation 5, open-circuit voltage V_{oc} and internal resistance R_0 are both functions of SOC. The functions $V_{oc}(SOC)$ and $R_0(SOC)$ are found using the experimental data in [20]. In this data, values for V_{oc} were measured and values R_0 were identified for 6 cells at discrete SOC values. This paper only uses the data for three cells (Cells 1, 3, and 6) as they showed the most consistent internal resistance trend over SOC. The V_{oc} and R_0 values were averaged and fit to a piece-wise linear function (Equation 6) and a polynomial function (Equation 7), respectively. Note that SOC does not reach 0 due to the limits of the laboratory testing.

$$V_{oc}(SOC) = \begin{cases} 2.61SOC + 2.93 & SOC \in [0.095, 0.19] \\ 0.94SOC + 3.24 & SOC \in (0.19, 1] \end{cases} \quad (6)$$

$$R_0(SOC) = 1.23SOC^6 - 4.34SOC^5 + 6.16SOC^4 - 4.52SOC^3 + 1.81SOC^2 - 0.37SOC + 0.066, \quad SOC \in [0.095, 1] \quad (7)$$

In addition to assuming that all cells are identical, we further assume that all cells are balanced at all times. This means that the SOC of each cell, and therefore V_{oc}, R_0, and V_{cell}, evolve identically through time, as determined by Equations 5, 6, and 7. Solving for cell current using Equations 3 and 5 yields

$$I_{cell}(t) = \frac{V_{oc}(SOC) - \sqrt{V_{oc}^2(SOC) - 4R_0(SOC)P_c}}{2R_0(SOC)} \quad (8)$$

V. Optimization Problem

The optimization problem is formulated as follows. Given the initial outage time t_0 and final outage time t_f, the goal is to minimize the objective function J for control $u(t)$, state $SOC(t)$, and time t

$$J = \int_{t_0}^{t_f} \dot{m}_f(dg(t))dt \quad (9)$$

The control $u(t)$ is constrained by the solar PV generation, load consumption, and the rated power of the LIB inverter, given the outage conditions defined in Section III-B

$$-\min\left(pv(t), P_{inv}\right) \leq u(t) \leq \min\left(l(t), P_{inv}\right), \quad \forall t \in [t_0, t_f] \quad (10)$$

The SOC dynamics are defined as

$$\dot{SOC}(t) = -\frac{1}{Q_{nom}} I_{cell}(t) \quad (11)$$

In this paper, the state is constrained at all times by

$$SOC_{LB} \leq SOC(t) \leq SOC_{UB}, \quad \forall t \in [t_0, t_f] \quad (12)$$

where $SOC_{LB} = 0.20$ and $SOC_{UB} = 0.85$, selected as reasonable bounds for microgrid LIB operation [22]. With the assumptions stated in Section III-B, the initial and final conditions of the SOC are

$$SOC(t_0) = SOC_{UB} \quad (13)$$

$$SOC(t_f) = SOC_f \quad (14)$$

VI. Pontryagin's Minimum Principle

PMP provides a set of necessary conditions for the optimal control $u^*(t)$ to minimize the objective function J in Equation 9 [23]. At each time $t \in [t_0, t_f]$:

1) The optimal control $u^*(t)$ minimizes the Hamiltonian

$$H(t, SOC^*, u^*, \lambda^*) \leq H(t, SOC^*, u, \lambda^*) \quad (15)$$

where the Hamiltonian is defined as $H(t, SOC, u, \lambda) = \dot{m}_f(dg(t)) + \lambda f(SOC, u)$.

2) The optimal costate $\lambda^*(t)$ satisfies the following

$$\dot{\lambda}^*(t) = -\frac{\partial H}{\partial SOC}(t, SOC^*, u^*, \lambda^*) \quad (16)$$

3) The optimal state $SOC^*(t)$ satisfies the following

$$\dot{SOC}^*(t) = \frac{\partial H}{\partial \lambda}(t, SOC^*, u^*, \lambda^*) = f(SOC^*, u^*) \quad (17)$$

In addition, the state constraints in Equations 13 and 14 must hold for the optimal state trajectory $SOC^*(t_0) = SOC_{UB}$ and $SOC^*(t_f) = SOC_f$.

A. Modification of Hamiltonian with state constraints

In order to guarantee the state constraints in Equation 12, the following additive penalty function $w(SOC)$ is introduced [7]

$$w(SOC) = \begin{cases} K & SOC > 0.85 \\ -K & SOC < 0.2 \\ 0 & o.w. \end{cases} \quad (18)$$

K is a constant chosen to be arbitrarily large. Any dispatch of the LIB where the SOC falls outside the specified bounds (i.e. discharging at low SOC or charging at high SOC) is penalized by the optimizer. In this paper, $K = 200$. The Hamiltonian is then modified to include this penalty function

$$H(t, SOC, u, \lambda) = \dot{m}_f(dg(t)) + (\lambda + w)\, f(SOC, u) \quad (19)$$

B. Costate dynamics

With the modified Hamiltonian in Equation 19, Equation 16 is rewritten as $\dot{\lambda}^*(t) = -(\lambda + w)\frac{\partial f(SOC,u)}{\partial SOC}$.

It remains to find $\frac{\partial f(SOC,u)}{\partial SOC}$. Using Equation 11, and considering that I_{cell} is a function of the independent functions of SOC, $V_{oc}(SOC)$ and $R_0(SOC)$

$$\frac{\partial f(SOC, u)}{\partial SOC} = \frac{\partial \dot{SOC}}{\partial SOC} = -\frac{1}{Q_{nom}}\left[\frac{\partial I_{cell}}{\partial V_{oc}}\frac{\partial V_{oc}}{\partial SOC} + \frac{\partial I_{cell}}{\partial R_0}\frac{\partial R_0}{\partial SOC}\right] \quad (20)$$

The partial derivatives $\frac{\partial V_{oc}}{\partial SOC}$ and $\frac{\partial R_0}{\partial SOC}$ are determined from Equations 6 and 7

$$\frac{\partial V_{oc}}{\partial SOC} = \begin{cases} 2.61 & SOC \in [0.095, 0.19] \\ 0.94 & SOC \in (0.19, 1] \end{cases} \quad (21)$$

$$\frac{\partial R_0}{\partial SOC} = 7.40SOC^5 - 21.69SOC^4 + 24.66SOC^3 - 13.55SOC^2 + 3.61SOC - 0.37, SOC \in [0.095, 1] \quad (22)$$

The partial derivatives $\frac{\partial I_{cell}}{\partial V_{oc}}$ and $\frac{\partial I_{cell}}{\partial R_0}$ are determined from Equation 8

$$\frac{\partial I_{cell}}{\partial V_{oc}} = \frac{1}{2R_0} - \frac{V_{oc}}{2R_0\sqrt{V_{oc}^2 - 4R_0P_c}} \quad (23)$$

$$\frac{\partial I_{cell}}{\partial R_0} = \frac{P_c}{R_0\sqrt{V_{oc}^2 - 4R_0P_c}} - \frac{V_{oc} - \sqrt{V_{oc}^2 - 4R_0P_c}}{2R_0^2} \quad (24)$$

C. Finding the optimal control

PMP allows for the reformulation of the finite horizon global optimization in Equation 9 in terms of the instantaneous

local minimization in Equation 15 and the differential equations for the state and costate [7]. As the evolution of state and costate are interdependent, and given the fixed, known initial state, it remains to find the initial costate λ_0^* to determine the optimal solution to Equation 9 which satisfies the state constraints.

The initial costate λ_0^* is found via shooting method using PMP and bisection line search on the initial costate value [7], shown in Algorithm 1. Given an initial guess for the initial costate value, λ_0, the PMP conditions are solved over the duration of the outage $[t_0, t_f]$, finding the optimal values for control, state, and costate at each time step. The final value of the state is compared to the target value, and the initial guess λ_0 is adjusted until convergence is reached and λ_0^* is obtained. In this paper, the initial bounds on the initial value of the costate λ_{LB} and λ_{UB} are set to -150 and -80 respectively, and the tolerance for convergence is set to $\epsilon = 0.01$, which results in convergence within 7 iterations.

Algorithm 1 Pseudocode for Optimal Control via Bisection Line Search on Initial Costate Value

Require: Outage load $l(t_0, ..., t_f)$, PV $pv(t_0, ..., t_f)$, target final SOC SOC_f, upper bound of initial costate λ_{UB}, lower bound of initial costate λ_{LB}, target final SOC tolerance ϵ
  while $|SOC(t_f) - SOC_f| > \epsilon$ **do**
    Set $\lambda_0 = (\lambda_{UB} - \lambda_{LB})/2$
    Solve the PMP conditions over $t \in [t_0, t_f]$ and retrieve optimal SOC trajectory $SOC(t_0), ...SOC(t_f)$
    if $|SOC(t_f) - SOC_f| < \epsilon$ **then**
      break
    else if $SOC(t_f) > SOC_f$ **then**
      Set $\lambda_{LB} = \lambda_0$
    else if $SOC(t_f) < SOC_f$ **then**
      Set $\lambda_{UB} = \lambda_0$
    end if
  end while
  Set $\lambda_0^* = \lambda_0$
  return Initial value of costate λ_0^*

The functions $\dot{SOC}$ and $\frac{\partial f(SOC,u)}{\partial SOC}$ are pre-computed as maps of SOC and u at discrete points within the operational bounds of the LIB. The range of SOC included in the maps is that of the functions $V_{oc}(SOC)$ and $R_0(SOC)$, and range of u included in the maps is selected to encompass the power limits set by P_{inv} and therefore the entire operating range of the LIB. In solving the PMP conditions, the function values are linearly interpolated between the map points. These function maps are shown as contour plots in Fig 3a and Fig. 3b, respectively.

VII. Results and Discussion

The PMP conditions are solved using the initial costate value obtained in Algorithm 1 for outage Phase 1 and outage Phase 3 in Table II for different values of $SOC(t_f) = SOC_f$. In each case, the resulting optimal state and control are then used to determine the total diesel consumption reduction M_{saved} and LIB capacity reduction S_{loss}. For M_{saved}, we calculate the percent change in diesel fuel consumed from the case when the LIB is not dispatched, to the case when the LIB is optimally dispatched $M_{saved}(SOC_f) = \frac{J(0)-J(u^*(t),SOC_f)}{J(0)}$, where $J(u^*(t), SOC_f)$ is the objective function in Equation 9 evaluated under the optimal LIB dispatch $u^*(t)$ for the condition $SOC(t_f) = SOC_f$, and $J(0)$ is the objective function evaluated when $u(t) = 0$ (independent of SOC_f). S_{loss}, in percentage of nominal capacity Q_{nom}, is determined using the semi-empirical model in [24], which models capacity loss as a function of Ampere-hour (Ah) throughput, the ratio of time spent in charge-sustaining mode, and temperature. Due to the constraints of this semi-empirical model, SOC_f is limited to the range $[0.2, 0.45]$ in this paper. Fig. 4 shows the optimal SOC trajectory for different values of SOC_f for Phase 1. This shows that the PMP conditions were successfully solved under the boundary conditions, as the values of SOC_f are reached at at the end of the outage. As SOC_f decreases from 0.45, the LIB discharges at a higher current initially, which has the effect of lowering the final SOC and increasing Ah throughput. However, as SOC_f approaches 0.2, the LIB has less opportunity to dispatch towards the end of the outage in order to maintain a lower SOC, decreasing Ah throughput. Fig. 5 shows the total diesel fuel consumption reduction and LIB cell capacity loss for different values of SOC_f for Phase 1 and Phase 3. For Phase 1, the reduction in cell capacity does not vary much across the SOC_f range, so in practical operation during this outage, SOC_f could be optimized to minimize diesel fuel consumption with minimal effect on degradation. In Phase 3, however, minimizing SOC_f has a clear effect on minimizing both diesel fuel consumption and

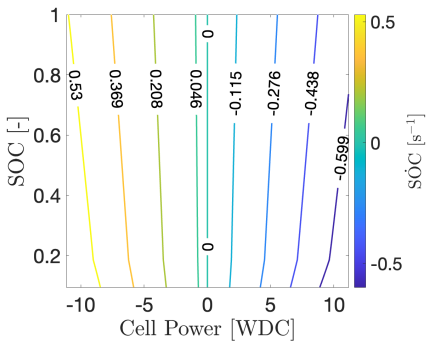

(a)

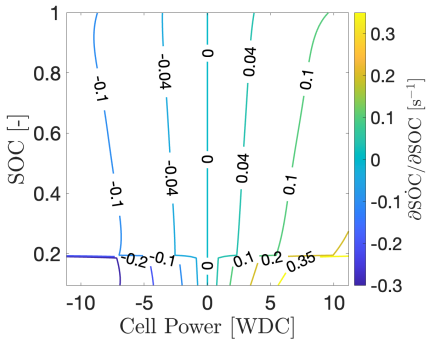

(b)

Fig. 3: Contour plots of (a) $\dot{SOC}$ and (b) $\partial\dot{SOC}/\partial SOC$, as functions of SOC and cell power P_c.

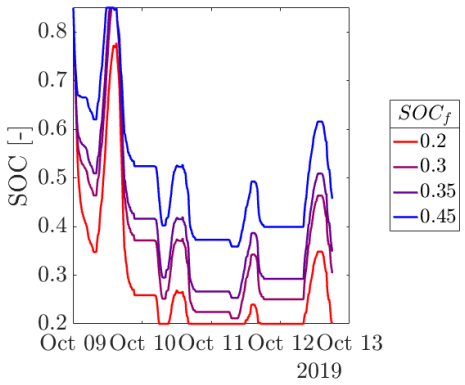

Fig. 4: Plot of optimal state trajectory $SOC^*(t)$ in Phase 1 for different values of final SOC, SOC_f. Redder lines denote final SOC closer to 0.2, while bluer lines denote final SOC closer to 0.45.

degradation. Additionally, the Phase 3 LIB degradation and diesel fuel consumption reduction are significantly lower than that of Phase 1 across all values of SOC_f. These results show that the optimal control and state, and the resulting capacity loss and diesel savings, are highly dependent on the initial and final conditions of the outage, even for different outage phases within the same PSPS.

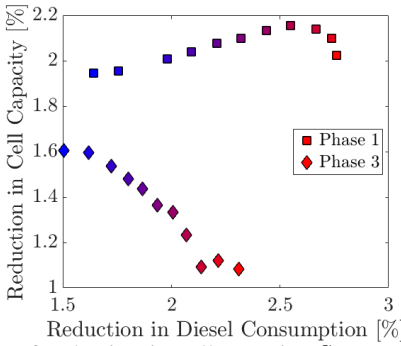

Fig. 5: Plot of reduction in cell capacity S_{loss} and reduction in diesel consumption M_{saved} in Phase 1 (square markers) and Phase 3 (diamond markers) for different values of final SOC $SOC_f \in [0.2, 0.45]$, in increments of 0.025. Redder markers denote final SOC closer to 0.2, while bluer markers denote final SOC closer to 0.45.

VIII. Conclusions

This paper presented a formulation for the energy management optimal control problem of a microgrid during islanded grid outage operation, where the LIB was modelled using an ECM informed by laboratory testing data. The necessary conditions for optimality in PMP were constructed using the ECM, and the optimal control was obtained for a variety of different boundary conditions, including variation of the final outage state. The resulting impacts on LIB degradation and diesel fuel consumption were compared across different outage phases. The results demonstrate that LIB degradation and diesel fuel consumption can be highly sensitive to outage conditions and the LIB operating constraints.

References

[1] A. Park Williams, J. T. Abatzoglou, A. Gershunov, J. Guzman-Morales, D. A. Bishop, J. K. Balch, and D. P. Lettenmaier, "Observed impacts of anthropogenic climate change on wildfire in California," *Earth's Future*, vol. 7, no. 8, pp. 892–910, 08 2019.

[2] B. Plumer, "A glimpse of America's future: Climate change means trouble for power grids," *New York Times*, 2021.

[3] CAL FIRE, "Top 20 deadliest california wildfires," CAL FIRE, Tech. Rep., 2020.

[4] I. Penn and P. Eavis, "PG&E Pleads Guilty to 84 Counts of Manslaughter in Camp Fire Case," *New York Times*, Jun 2020. [Online]. Available: https://www.nytimes.com/2020/06/16/business/energy-environment/pge-camp-fire-california-wildfires.html

[5] Office of Electricity Delivery and Energy Reliability Smart Grid R&D Program, "DOE microgrid workshop report," United States Department of Energy, Tech. Rep., 2011.

[6] Pacific Gas & Electric, "PG&E public safety power shutoff (PSPS) report to the CPUC October 9-12, 2019 de-energization event," Pacific Gas & Electric, Tech. Rep., 2020.

[7] S. Onori, L. Serrao, and G. Rizzoni, *Hybrid Electric Vehicles*. Springer London, 2016.

[8] L. Serrao, S. Onori, A. Sciarretta, Y. Guezennec, and G. Rizzoni, "Optimal energy management of hybrid electric vehicles including battery aging," in *Proceedings of the 2011 American Control Conference*, 2011, pp. 2125–2130.

[9] N. Kim, S. Cha, and H. Peng, "Optimal control of hybrid electric vehicles based on Pontryagin's minimum principle," *IEEE Transactions on Control Systems Technology*, vol. 19, no. 5, pp. 1279–1287, 2011.

[10] Z. Song, X. Zhang, J. Li, H. Hofmann, M. Ouyang, and J. Du, "Component sizing optimization of plug-in hybrid electric vehicles with the hybrid energy storage system," *Energy*, vol. 144, 2018.

[11] A. Serpi, M. Porru, and A. Damiano, "An optimal power and energy management by hybrid energy storage systems in microgrids," *Energies*, vol. 10, no. 11, 2017.

[12] N. Zargari, Y. Levron, and J. Belikov, "Optimal control of energy storage devices based on Pontryagin's minimum principle and the shortest path method," in *2019 IEEE PES Innovative Smart Grid Technologies Europe (ISGT-Europe)*, 2019, pp. 1–5.

[13] N. R. Chowdhury, R. Ofir, N. Zargari, D. Baimel, J. Belikov, and Y. Levron, "Optimal control of lossy energy storage systems with nonlinear efficiency based on dynamic programming and Pontryagin's minimum principle," *IEEE Transactions on Energy Conversion*, vol. 36, no. 1, pp. 524–533, 2021.

[14] J. He, C. Shi, T. Wei, X. Peng, and Y. Guan, "Hierarchical optimal energy management strategy of hybrid energy storage considering uncertainty for a 100% clean energy town," *Journal of Energy Storage*, vol. 41, p. 102917, 2021.

[15] D. Carter, D. Saucedo, J. Zoellick, and al., "Demonstrating a secure, reliable, low-carbon community microgrid at the Blue Lake Rancheria," Schatz Energy Research Center, Tech. Rep., 2019.

[16] M. Mueller-Stoffels, J. VanderMeer, H. Schaede, L. Miranda, and D. L. et al., "Diesel generator fuel consumption under dynamic loading," Alaska Center for Energy and Power, Tech. Rep., 2017.

[17] Humboldt State University, "Microgrid provides critical services throughout northern CA during power shutdown," *Newswise*, 2019.

[18] Pecan Street Inc, "Pecan Street Dataport," 2020. [Online]. Available: https://www.pecanstreet.org/dataport/

[19] National Renewable Energy Laboratory, "System Advisor Model Version 2020.11.29 (SAM 2020.11.29)," Golden, Colorado, USA.

[20] E. Catenaro, D. M. Rizzo, and S. Onori, "Experimental analysis and analytical modeling of enhanced-Ragone plot," *Applied Energy*, vol. 291, p. 116473, 2021.

[21] *MPS-250 800V Inverter*, Dynapower. [Online]. Available: https://www.dynapower.com/products/energy-storage-solutions/behind-the-meter-energy-storage/mps-250-800v

[22] D. Tran and A. M. Khambadkone, "Energy management for lifetime extension of energy storage system in micro-grid applications," *IEEE Transactions on Smart Grid*, vol. 4, no. 3, pp. 1289–1296, 2013.

[23] H. P. Geering, *Optimal control with engineering applications*. Berlin: Springer, 2009.

[24] A. Cordoba-Arenas, S. Onori, Y. Guezennec, and G. Rizzoni, "Capacity and power fade cycle-life model for plug-in hybrid electric vehicle lithium-ion battery cells containing blended spinel and layered-oxide positive electrodes," *J. Power Sources*, vol. 278, 2015.